43rd AIAA Aerospace Sciences Meeting and Exhibit, January 10–13, Reno, Nevada.

Time-Accurate Three-Dimensional Simulations of Synthetic Jets in Quiescent Air

Rupesh B. Kotapati[*] and Rajat Mittal[†]
The George Washington University, Washington, DC 20052, USA

The evolution of three-dimensional synthetic jet into initially quiescent air is studied by direct numerical simulations of incompressible Navier-Stokes equations. The numerical scheme uses a second-order accurate semi-implicit fractional step method on Cartesian grids. Simulations are carried out at a Reynolds number of 1150 and Stokes number of 17. The results indicate that near the jet exit plane, the flowfield is dominated by the formation of counter-rotating vortex pairs that breakdown due to the onset of spanwise instabilities and transition to fully developed turbulent jet at short distances from the orifice. Detailed spectral analysis is carried out in three regions — near exit plane, slot region and jet cavity — to study the transition to turbulence. The results from the simulations are compared with the measurements to assess various aspects of the predictions. The phase-averaged and the time-averaged velocity fields near the exit plane are validated with the measurements and the computed flowfield inside the slot and the cavity is examined in detail.

Nomenclature

Re	Reynolds number, $Re = \bar{V}_j d/\nu$
St	Stokes number, $St = \sqrt{2\pi f d^2/\nu}$
$\bar{V}_j$	Average velocity over the discharge phase of the cycle, $\bar{V}_j = \frac{2}{AT}\int_A \int_0^{T/2} u_0(x,z,t)\, dt\, dA$, m/s
A	Exit area of the jet orifice, m^2
d	Jet orifice width, m
f	Forcing frequency, Hz
T	Forcing period, $T = 1/f$
t	Time
u_0	Velocity at the exit plane of the orifice, m/s
V_0	Velocity amplitude at which the lower boundary is forced in the cavity, m/s

Subscripts

i	Directional index, $i = 1, 2, 3$

Symbols

ν	Kinematic viscosity, m^2/s
ϕ	Phase angle, $\phi = 2\pi t/T$, degrees

---

[*] Doctoral Student, Department of Mechanical and Aerospace Engineering; rupesh@gwu.edu, Student Member AIAA.

[†] Associate Professor, Department of Mechanical and Aerospace Engineering; mittal@gwu.edu, Senior Member AIAA.

I. Introduction

Synthetic jet devices have emerged as versatile actuators with potential applications ranging from thrust vectoring of jets[1] to triggering turbulence in boundary layers[2,3,4] and active flow control.[5,6,7,8] The versatility of these actuators is primarily attributed to the following reasons: (a) they provide unsteady forcing that is more effective than steady or pulsed forcing, (b) since the jets are synthesized from the working fluid, complex fluid circuits are not required, and (c) actuation frequency can usually be tuned to a particular flow configuration. A typical synthetic jet actuator consists of a jet orifice opposed on one side by an enclosed cavity. Time-periodic changes in volume of the cavity cause a stream of vortices to be generated at the edges of the orifice, imparting finite momentum into the surrounding fluid, although the net mass-flux through the orifice is zero. Interaction of these vortical structures with the external flow field has been found to cause formation of closed recirculation regions with the modification of the flow boundary, thereby causing global modifications to the base flow on scales larger than the characteristic length scales of the synthetic jets themselves.[9,10]

A variety of experimental techniques have been used in the development of zero-net-mass-flux (ZNMF) actuators. One of the earliest investigations of streaming motions is due to Meissner,[11] who studied the attenuation of very high-frequency sound waves within the body of the fluid. Ingard and Labate[12] studied the impedance of orifices by applying an orifice plate to a circular tube driven by sound waves and reported the effects of circulation caused by acoustic streaming. Andres and Ingard[13] looked at acoustic streaming at high Reynolds numbers and investigated the attenuation of the transmitted sound waves near solid boundaries due to viscous effects. Mednikov and Novitskii[14] used an oscillating piston and bellows mechanism to produce ZNMF jets from a resonant cavity. Lebedeva[15] transmitted high amplitude sound waves through a pipe opposed with an orifice plate to create a round jet and investigated acoustic streaming in the vicinity of the orifices. Sheen, Lawrence and Raptis[16] employed cavitation-controlled ultrasonic agitators to create streaming motions in water. Smith and Glezer[17] synthesized a nominally two-dimensional jet by oscillatory motion of a flexible diaphragm in a sealed cavity and investigated its near-field formation and evolution by measuring the cross stream distributions of the velocity components using hot-wire anemometry. In a recent workshop, Yao *et al.*[18] presented velocity measurements on synthetic jets in quiescent air obtained using time-periodic oscillation of a wall-mounted piezo-electric diaphragm in an enclosed cavity. In this experiment, velocity measurements from three different techniques, namely, hot-wire anemometry, Laser Doppler Velocimetry (LDV) and Particle Image Velocimetry (PIV), documented the synthetic jet flowfield.

A limited amount of numerical work on synthetic jets in the absence of cross-flow has been reported in the literature. The first of them is by Kral *et al.*,[19] who reported two-dimensional incompressible calculations of both laminar and turbulent synthetic jets, the latter obtained by the solution of unsteady Reynolds-averaged Navier-Stokes (URANS) equations with Spalart-Allmaras (SA) one-equation turbulence closure. Three different analytic velocity profiles at the orifice exit were examined and the flow within the cavity was not modeled. Turbulent solutions showed good agreement with the measured mean velocity profiles. However, further away from the jet, vortices in the turbulent simulations were smeared by turbulent diffusion and the lack of three-dimensionality in the laminar predictions failed to capture the breakup of the vortex train observed in the experiments. Rizzetta, Visbal and Stanek[20] investigated two- and three-dimensional flowfields of nominally planar synthetic jets using direct numerical simulations (DNS) of unsteady compressible Navier-Stokes equations. The motion of the diaphragm in the cavity was modeled by sinusoidally varying the position of the lower boundary. When internal cavity flow became periodic after several cycles, the velocity profile at the slot exit was recorded at each time step for one complete cycle and specified as a boundary condition at the slot exit in the subsequent cycles without having to model the cavity thereafter. The exterior flow field was then constructed using high-order compact-difference schemes in conjunction with non-dispersive spatial filters by enforcing symmetry conditions along the jet centerline that precluded asymmetric interactions between vortices across the centerline. Three-dimensionality in their simulations helped capture the breakdown of external flow into a turbulent jet, a phenomenon observed in the experiments, but missed in any strictly two-dimensional calculations. Mallinson, Hong and Reizes[21] made similar observations by comparing their experimental measurements with their URANS simulations of round jet, with $\kappa - \epsilon$ turbulence closure, performed along the same lines as Kral *et al.*[19]

Recently, Lee and Goldstein[22] reported two-dimensional computations of an array of synthetic jets using an alternate direct numerical simulation method based on imposing localized body forces to represent velocity at solid boundaries. The computations were carried out with inconsistent boundary conditions from those of the experiments which resulted in ejected vortices impacting the top boundary and flowing back into near-field to affect the translation of newly formed vortex pairs. Utturkar *et al.*[23] carried out detailed parametric two-dimensional computations to study the effects of variation in the operational parameters such as diaphragm amplitude and slot dimensions as well as external flow characteristics. The authors proposed and validated the jet formation criterion $Re/St^2 > K$, where the constant K is around 2 and 0.16 for two-dimensional and axisymmetric synthetic jets, respectively.

In the study reported here, the unsteady evolution of a transitional synthetic jet in the absence of cross-flow is investigated by time-accurate three-dimensional direct numerical simulations of incompressible Navier-Stokes equations on Cartesian grids at $Re = 1150$. The study models the flow inside the cavity using an oscillatory velocity boundary condition prescribed at the bottom of the cavity in order to generate a natural flow at the slot exit. The flow configuration is similar to the one studied by Yao *et al.*[18] described earlier and the results from the computations are validated using their measurements. The paper is organized as follows. First, the flow configuration used in the computations is summarized. This is followed by the description of the equations of motion governing the flow field and the numerical methodology used in the computations. Finally, the results obtained from the computations are presented and discussed.

II. Simulation Overview

A. Flow Configuration

The geometry used in the computations is relatively simple as compared to the apparatus used in the experiments. In the computations, the shape of the cavity is approximated to be a rectangular box without taking into consideration the finer details that make up the interior of the cavity used in the experiments. Previous numerical studies by Utturkar *et al.*[23] on the sensitivity of the synthetic jets to the design of the jet cavity have shown that the large differences in the internal cavity flow, with symmetric forcing, do not translate into similar differences in the external flow. A schematic of the geometry used in the simulations is shown in figure 1 on the following page and it consists of a rectangular cavity connected to the external domain through a narrow rectangular orifice or slot. The origin of the coordinate system is fixed in the jet exit plane along the jet centerline in the symmetry plane. Note that x, y and z are in the cross stream, streamwise and spanwise directions, respectively. While the cavity is defined by the width (W) and height (H), the jet slot is characterized by width (d) and height (h). Care has been taken to match, as closely as possible, the geometrical parameters such as the ratios h/d and W/d used in the computations with those in the experiments. However, it should be noted that cavity height (H) and the slot height (h) can not be properly defined in the experiments of Yao *et al.*[18] as the width varies gradually from W in the cavity to d at the slot exit. Also, it should be noted that the experiments were carried out using a finite aspect ratio jet slot (aspect ratio of 28) in an enclosed box causing the measurements in the symmetry plane to be affected by the end-wall effects of the slot and domain size effects within short distances from the jet exit plane. In the present study, the ratios h/d, W/d and H/d are chosen to be 2.6, 2.45 and 4.95, respectively. In the experiments, the fluid is periodically expelled from and entrained into the cavity by an oscillating diaphragm mounted on one of the side walls of the cavity. The diaphragm oscillation is modeled in the computations by specifying sinusoidal velocity boundary condition $V_0 sin(2\pi f t)$ at the bottom of the cavity. While V_0 is determined by trying to match Re in the experiments, the frequency f is determined by matching St used in the experiments. The effects of three-dimensionality, grid resolution and spanwise domain size on the predictions are studied systematically by a sequence of computations detailed in table 1. Figure 1 shows the boundary conditions used in the computations. An outflow velocity boundary condition is prescribed on the

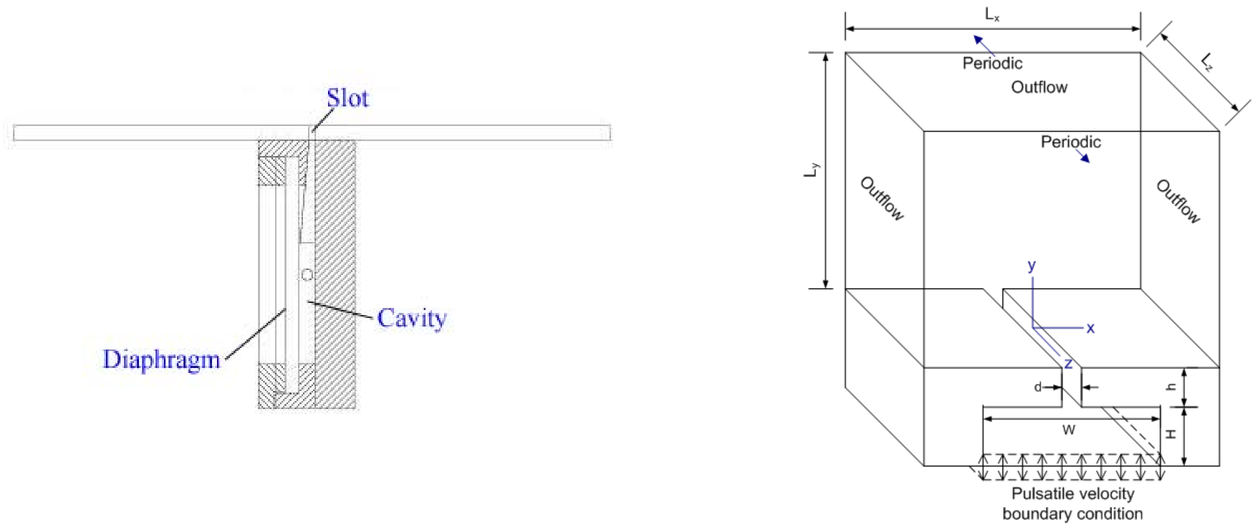

(a) Experimental setup[18]

(b) Computational domain

Figure 1. Schematic of the geometry.

east, west and north boundaries to allow them to respond freely to the flow created by the jet, and periodic boundary conditions are prescribed in the spanwise (z) direction. The periodicity in the span is intended to model the spanwise homogeneous flow through a slot with an infinite spanwise extent. Figures 2a and 2b show, respectively, the domain mesh and an x-y slice of a typical three-dimensional mesh used in the slot region in the computations. Grids used in the current work are non-uniform in both x- and y-directions, and uniform in the spanwise (z) direction. Sufficient clustering is provided in the slot-region (figure 2c) along x- and y-directions to resolve the vortex structures that form at the slot exit, as well as the shear layer in the slot. Typically 32x55 grid points are used across the slot. A time step corresponding to 14,000 steps per cycle is employed in the calculations. The computations are performed on a single 2.8 GHz Pentium® 4 processor-based workstation and the CPU time incurred for Case 4 was around 270 hours per cycle. The three-dimensionality in the solution is instigated by introducing a small sinusoidal spatial perturbation in the w-velocity over a few hundred time-steps in the first cycle, and thereafter the three-dimensionality is

Table 1. Various computations reported in the current study. L_x, L_y and L_z denote the domain size in x-, y- and z-directions, respectively. N_x, N_y and N_z denote the number of cells in x-, y- and z-directions, respectively.

Case	L_x x L_y x L_z	N_x x N_y x N_z	Cycles averaged
1	40d x 42.45d x 3.0d	132 x 220 x 16	10–15
2	40d x 42.45d x 3.0d	132 x 220 x 24	9–15
3	40d x 42.45d x 4.5d	132 x 220 x 24	9–13
4	60d x 60d x 6.0d	142 x 230 x 48	5–7

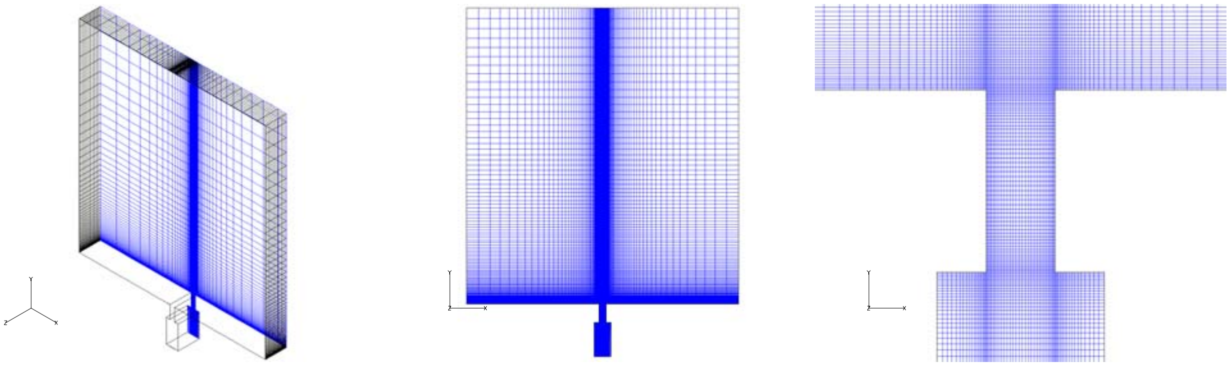

(a) Domain grid.

(b) Grid in the x-y plane.

(c) Grid in the slot region.

Figure 2. Typical computational mesh used in the simulations.

allowed to develop on its own through the inherent instability of the flow. The solution was allowed to evolve for several cycles to eliminate transient effects, and only the later cycles detailed in table 1 were used in the computation of flow statistics defined in § C.

B. Numerical Methodology

The evolution of zero-net-mass-flux (ZNMF) synthetic jets from a cavity in the absence of crossflow is modeled by the unsteady, incompressible Navier-Stokes equations, written in tensor form as

$$\frac{\partial u_i}{\partial x_i} = 0 \tag{1}$$

$$\frac{\partial u_i}{\partial t} + \frac{\partial (u_i u_j)}{\partial x_j} = -\frac{\partial p}{\partial x_i} + \frac{1}{Re}\frac{\partial^2 u_i}{\partial x_j x_j} \tag{2}$$

where the indices, $i = 1, 2, 3$, represent the x_1 (x), x_2 (y) and x_3 (z) directions, respectively, p is the pressure and the components of the velocity vector $\boldsymbol{u}$ are denoted by u_1 (u), u_2 (v) and u_3 (w), respectively. The equations are non-dimensionalized with the appropriate length and velocity scales where Re represents the Reynolds number. The Navier-Stokes equations are discretized using a cell-centered, collocated (non-staggered) arrangement of the primitive variables $(\boldsymbol{u}, p)$. In addition to the cell-center velocities $(\boldsymbol{u})$, the face-center velocities $(\boldsymbol{U})$, are also computed. Similar to a fully staggered arrangement, only the component normal to the cell-face is calculated and stored. The face-center velocity is used for computing the volume flux from each cell. The advantage of separately computing the face-center velocities has been initially proposed by Zang, Street and Koseff[24] and discussed in the context of the current method in Ye *et al.*[25] The equations are integrated in time using a second-order accurate fractional step method. In the first step, the momentum equations without the pressure gradient terms are first advanced in time. In the second step, the pressure field is computed by solving a Poisson equation. A second-order Adams-Bashforth scheme is employed for the convective terms while the diffusion terms are discretized using an implicit Crank-Nicolson scheme which eliminates the viscous stability constraint. The pressure Poisson equation is solved with a Krylov-based approach. The solver uses weighted-averaging of second order central difference scheme and second order upwind scheme for the discretization of convective face velocities. The QUICK scheme[26] obtained by setting the weighting factor $\theta = 1/8$ is used in the present computations. Care has been taken to ensure that the discretized equations satisfy local and global mass conservation constraints as well as pressure-velocity compatibility relations. The code has been rigorously validated by comparisons of several test cases against established experimental and computational data. Details have been presented elsewhere.[27]

C. Data Reduction

The various averaging operations employed in the computation of flow statistics in the current study are described as follows. For a generic flow variable $f(\boldsymbol{x}, t)$, the time-mean over M cycles is defined as

$$\langle f\rangle(x, y) = \frac{1}{L_z}\frac{1}{MT}\int_{t_0}^{t_0+MT}\int_0^{L_z} f(\boldsymbol{x}, t)\, dz\, dt, \tag{3}$$

where t_0 corresponds to the initial time of the averaging process. Deviation from the time-mean is computed as

$$f'(\boldsymbol{x}, t) = f(\boldsymbol{x}, t) - \langle f\rangle. \tag{4}$$

In addition, for flows with imposed periodic forcing such as the one under investigation here, it is useful to compute a phase average.[28] The phase average over M cycles is defined as

$$F(x, y, t) = \frac{1}{L_z}\frac{1}{M}\sum_{n=0}^{M-1}\int_0^{L_z} f(\boldsymbol{x}, t + nT)\, dz. \tag{5}$$

Deviation from this phase average is referred to as 'turbulent' fluctuation and is computed as

$$f''(\boldsymbol{x}, t) = f(\boldsymbol{x}, t) - F. \tag{6}$$

The phase average F represents the time-varying coherent (or deterministic) part of the flow and primarily contains time scales directly associated with the organized wave motion. The deviation from the phase average (f'') represents the non-deterministic motions and therefore this decomposition provides a means for extracting scales that are associated with the pulsation from a background field of finite turbulent fluctuations.

III. Results and Discussion

Contours of phase-averaged spanwise vorticity (Ω_z) obtained for Case 4 are plotted in figure 3 on the next page as a function of phase angle ϕ for every 45^o. Phase angle $\phi = 0^o$ is arbitrarily chosen to correspond to the commencement of the upward motion of the diaphragm modeled here by the pulsatile velocity boundary condition at the bottom of the cavity. The horizontal lines seen in the background above the jet exit plane are separated from each other and from the slot exit by distance d. At $\phi = 0^o$, the plot shows some remnants of the previous vortex pair in the near-field and the separation of the shear layer in the interior of the slot caused by the suction of the ambient fluid into the cavity before the upward motion of the diaphragm began. The plot also shows the presence of corner vortices in the cavity. At 45^o in phase, a new vortex pair rolls up at the edge of the slot and its size is of the order of the slot width. The plot also shows separation of the shear layer at the inner edges of the slot. When the rollup process is completed at the maximum-expulsion phase of 90^o, the vortex pair detaches from the exit plane and grows in size as it advects downstream. At $\phi = 135^o$, small-scale structures begin to appear on the rim of vortex pairs. Also, the rollup of the shear layer at the inner lip of the slot advects downstream leading to Kelvin-Helmholtz-type instabilites that mark the first stage in the transition process. The expulsion phase is completed and the injestion phase is commenced at $\phi = 180^o$, by which time the vortex pair has advected sufficiently downstream ($y/d \approx 4$) that it is not affected by the suction of ambient fluid into the cavity. At this juncture, the vortex pair loses coherence and begins to mix with the ambient fluid. At $\phi \approx 225^o$, the vortices lose their individual identity, and the suction generates vortex rollup in the interior of the cavity. At maximum-ingestion phase of 270^0, the

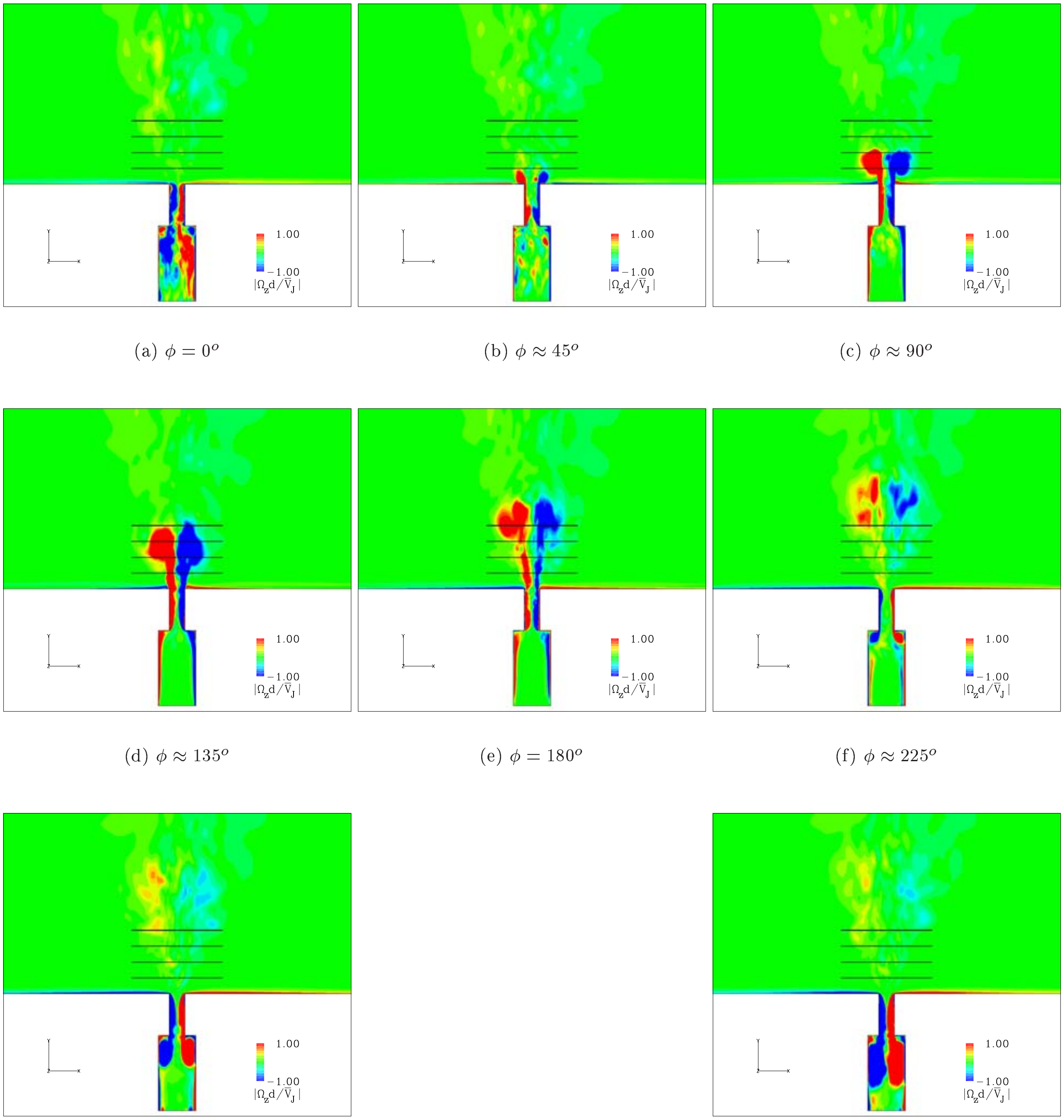

(a) $\phi = 0^o$

(b) $\phi \approx 45^o$

(c) $\phi \approx 90^o$

(d) $\phi \approx 135^o$

(e) $\phi = 180^o$

(f) $\phi \approx 225^o$

(g) $\phi \approx 270^o$

(h) $\phi \approx 315^o$

Figure 3. Contours of phase-averaged spanwise vorticity (Ω_z) at various phase angles obtained for Case 4.

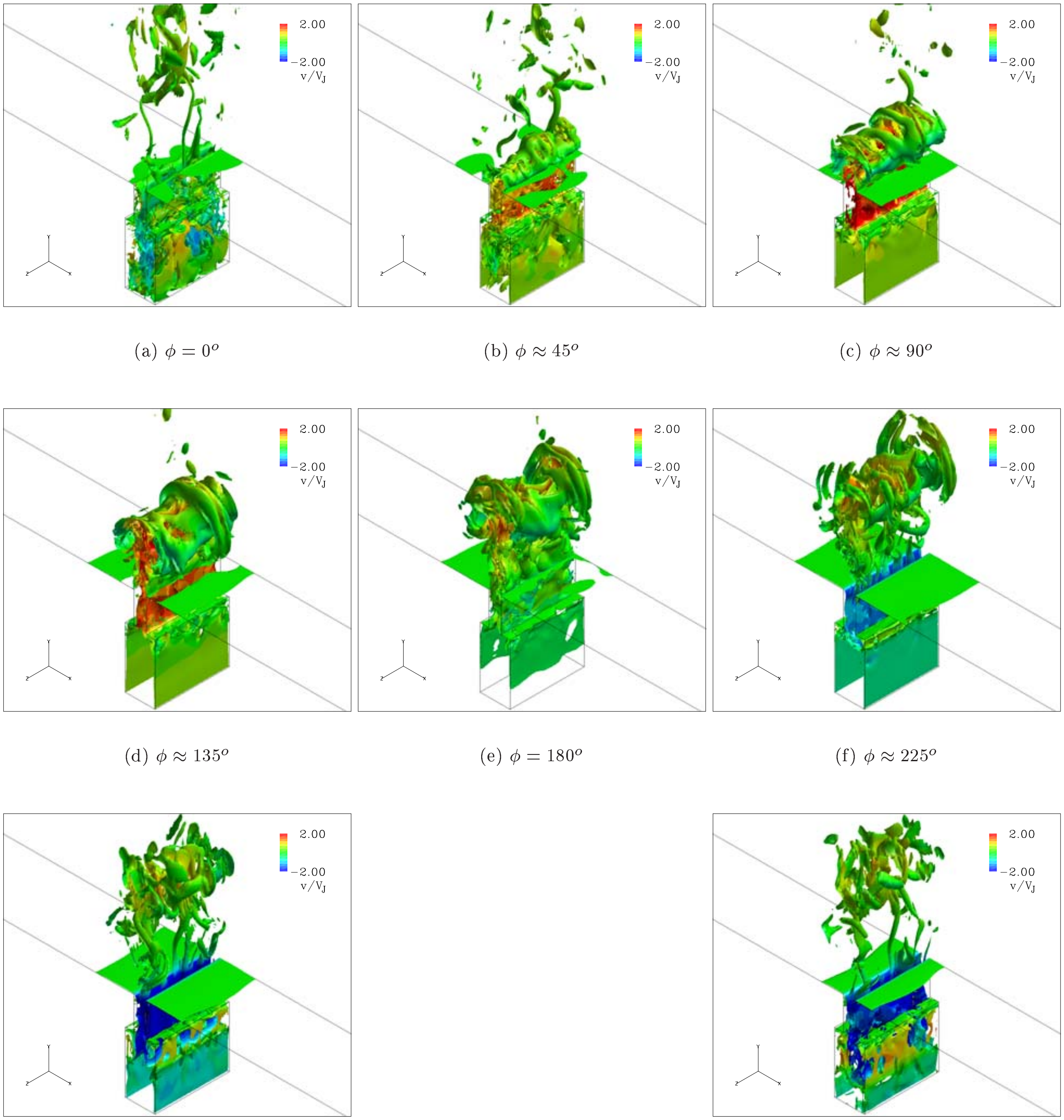

(a) $\phi = 0^o$

(b) $\phi \approx 45^o$

(c) $\phi \approx 90^o$

(d) $\phi \approx 135^o$

(e) $\phi = 180^o$

(f) $\phi \approx 225^o$

(g) $\phi \approx 270^o$

(h) $\phi \approx 315^o$

Figure 4. Isosurfaces of instantaneous vorticity magnitude colored by v-velocity at various phase angles obtained for Case 4 during the seventh cycle.

mixing of the primary vortex pair is complete, resulting in a fully developed turbulent jet beyond $y/d = 3$. The vortex pair inside the cavity as seen at $\phi = 315^o$ starts to grow in size while it descends and engulfs the cavity before the next cycle is begun.

Figure 4 on the preceding page depicts a sequence of plots of isosurfaces of vorticity magnitude obtained for Case 4 during the seventh cycle for every 45^o in phase. The figure clearly depicts the process of transition of the primary vortex pair into a fully developed turbulent jet. At the maximum-expulsion phase of 90^o, the plot shows the presence of spanwise-periodic counter-rotating rib-like vortical structures in the streamwise direction. These streamwise rollers coil around the cores of the primary vortex pair. As the primary vortex pair advects downstream in the subsequent phases, these spanwise instabilities undergo rapid amplification leading to breakdown of the primary vortex pair due to three-dimensional vortex stretching and complete mixing of the vortices with the ambient fluid within a short distance from the orifice. This process of transition is consistent with the phase-locked smoke visualizations of a synthetic jet at $Re = 766$ by Smith and Glezer.[17]

Plot of phase-averaged time history of v-velocity obtained from the computations along the vertical centerline at $y/d = 0.1$ is shown in figure 5. Also included in this plot are the PIV and the LDV measurements of Yao *et al.*[18] Whereas the computed results show grid convergence, the PIV and LDV measurements show differences amongst themselves with respect to the peak amplitudes and alignment in phase. Even though the PIV data align with the computations at maximum-ingestion phase ($\phi = 270^o$), the maximum-expulsion in the PIV measurements leads the computational results by as much as 14^o in phase. Nevertheless, in the comparisons of cross stream distributions of various velocity profiles, the results from the simulations at maximum-expulsion phase are validated against the PIV data at $\phi = 90^o$ rather than at $\phi = 76^o$ as the agreement is better at $\phi = 90^o$ (not shown here) than at $\phi = 76^o$.

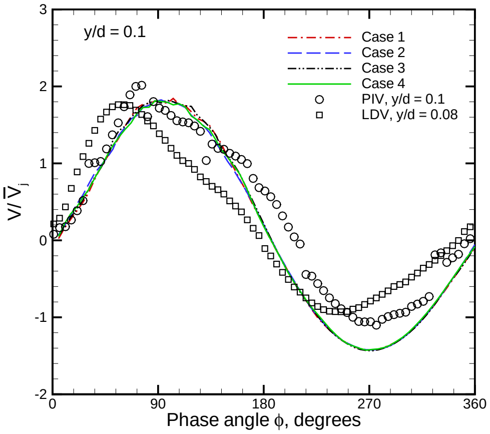

Figure 5. Plot of phase-averaged v-velocity along the vertical centerline at $y/d = 0.1$.

Figure 6 on the following page shows the plots of phase-averaged v-velocity profile along the centerline $x/d = 0.0$ above the jet exit plane at phase angles $\phi \approx 90^o$ and $\phi \approx 270^o$. At the maximum-expulsion phase ($\phi \approx 90^o$), the computed velocity profiles closely agree with the measurements for $y/d \geq 2$, and for $y/d < 2$ the magnitude of the maximum centerline velocity in the computations takes a slightly lower value than the measurements. This difference can be attributed to the end wall effects in the experiments that cause the fluid to accelerate between shear layers formed at the slot end walls. At the maximum-ingestion phase, results from the computations match the measurements until up to $y/d = 4$ beyond which the computations show higher velocity magnitude than the measurements. Figure 7 on page 11 shows the comparisons with the measurements of the cross stream distributions of phase-averaged u- and v-velocity profiles above the

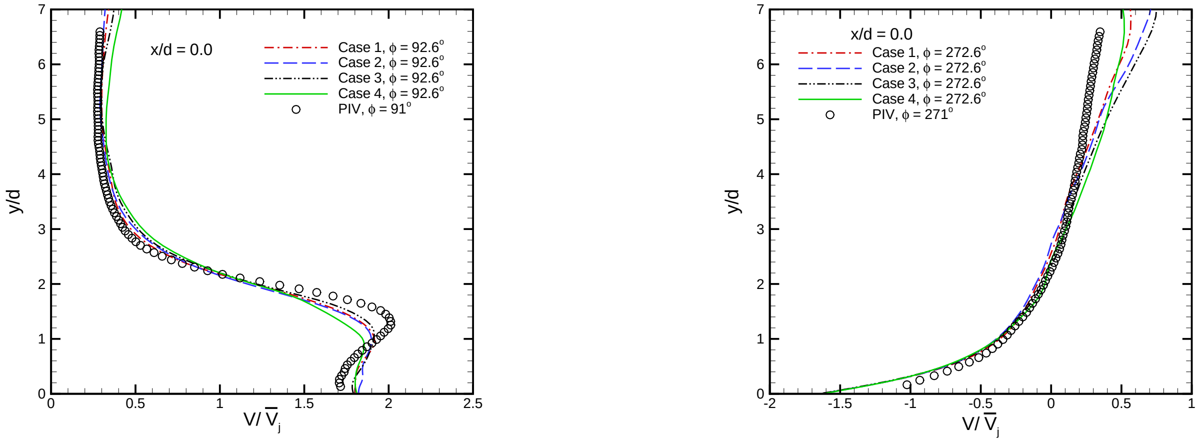

Figure 6. Plot of phase-averaged v-velocity profile along the vertical centerline $x/d = 0.0$ above the jet exit plane at phase angles $\phi \approx 90^o$ and $\phi \approx 270^o$.

jet exit plane at $y/d = 0.787, 1.575$ and 2.362 at $\phi \approx 90^o$. Except for the lower values of the maxima and the minima in the U-velocity at $y/d = 0.787$ and the V-velocity at $y/d = 1.575$ as compared to the measurements, the computed profiles closely agree with the experimental measurements. Similar profiles at phase angle $\phi = 270^o$ is shown in figure 8 on page 12. At this maximum-ingestion phase, the velocity profiles follow the general trend seen in the measurements. However, the magnitude of the computed U-velocity outside the core region of the jet at all three stations takes a higher value than the measurements, implying greater entrainment in the computed flow fields than that observed in the experiments. Also, the magnitude of V-velocity along the centerline at $y/d = 0.787$ is higher in the computations as compared to the measurements. The jitter seen in the computed V-velocity profiles in the core region at $y/d = 1.575$ and $y/d = 2.362$ is attributed to the lack of a very large sample size as in the experiments for the computation of flow statistics.

Based on these validations in the near-field, we extend the ongoing study to gain insight into the flow field inside the slot and the cavity where experimental measurements are not possible due to limitations on the instrumentation. Figure 9 on page 13 shows the cross stream distributions of phase-averaged v-velocity profiles from the computations at $\phi \approx 90^o$ and $\phi \approx 270^o$ at five different stations. Whereas the profiles at $y/d \approx -1$ and -2 correspond to stations in the slot, the profiles at $y/d \approx -3$, -4 and -5 correspond to stations in the cavity. At $\phi \approx 90^o$, the cross stream distributions at $y/d \approx -5$ and -4 resemble developed channel flow profiles. The computed profiles at $y/d \approx -3$ show reverse flow near the walls implying the presence of the corner eddy in the cavity. The acceleration of the fluid from the cavity into the slot is expected to cause laminarization of the flow as seen in the profiles at $y/d \approx -2$. The profiles at this station also show reverse flow caused by separation at the inner edges of the slot. However, the profiles become more uniform at $y/d \approx -1$ before the flow exits out of the slot. At the maximum-ingestion phase ($\phi = 270^o$), as seen in the profiles at $y/d \approx -1$, the suction at the slot has a stabilizing effect on the ambient fluid as it accelerates into the narrow slot and so we expect the flow to be less turbulent. This aspect of the flow is looked at in more detail using spectral analysis discussed later. However, the flow recovers the developed profile at $y/d \approx -2$ before it exits out of the slot and rolls up into a vortex pair in the cavity. Profiles at $y/d \approx -3$ and -4 show recirculation regions characterized by the vortex pair in the cavity. At $y/d \approx -5$, the profiles do not show any flow reversals as this station is not within the reach of the vortex pair at this instant in phase.

Figure 10 on page 13 shows the comparisons of the computed time-averaged v-velocity profiles with the experiments along the vertical centerline above the jet exit plane. The plot shows consistently lower values in

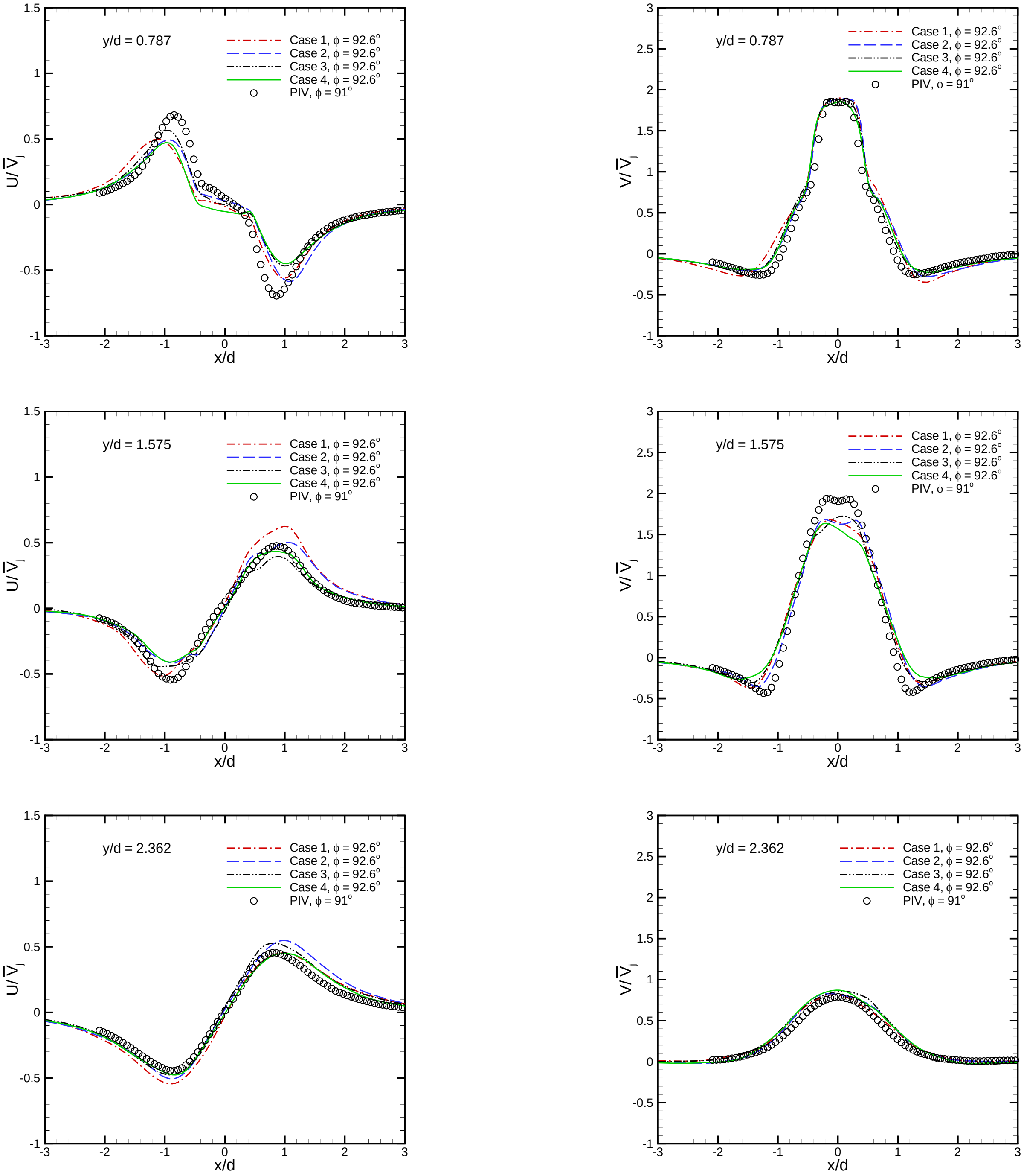

Figure 7. Plot of phase-averaged u**- and** v**-velocity profiles along the horizontal lines** $y/d = 0.787$**,** $y/d = 1.574$ **and** $y/d = 2.362$**, above the jet exit plane at phase angle** $\phi \approx 90^o$**.**

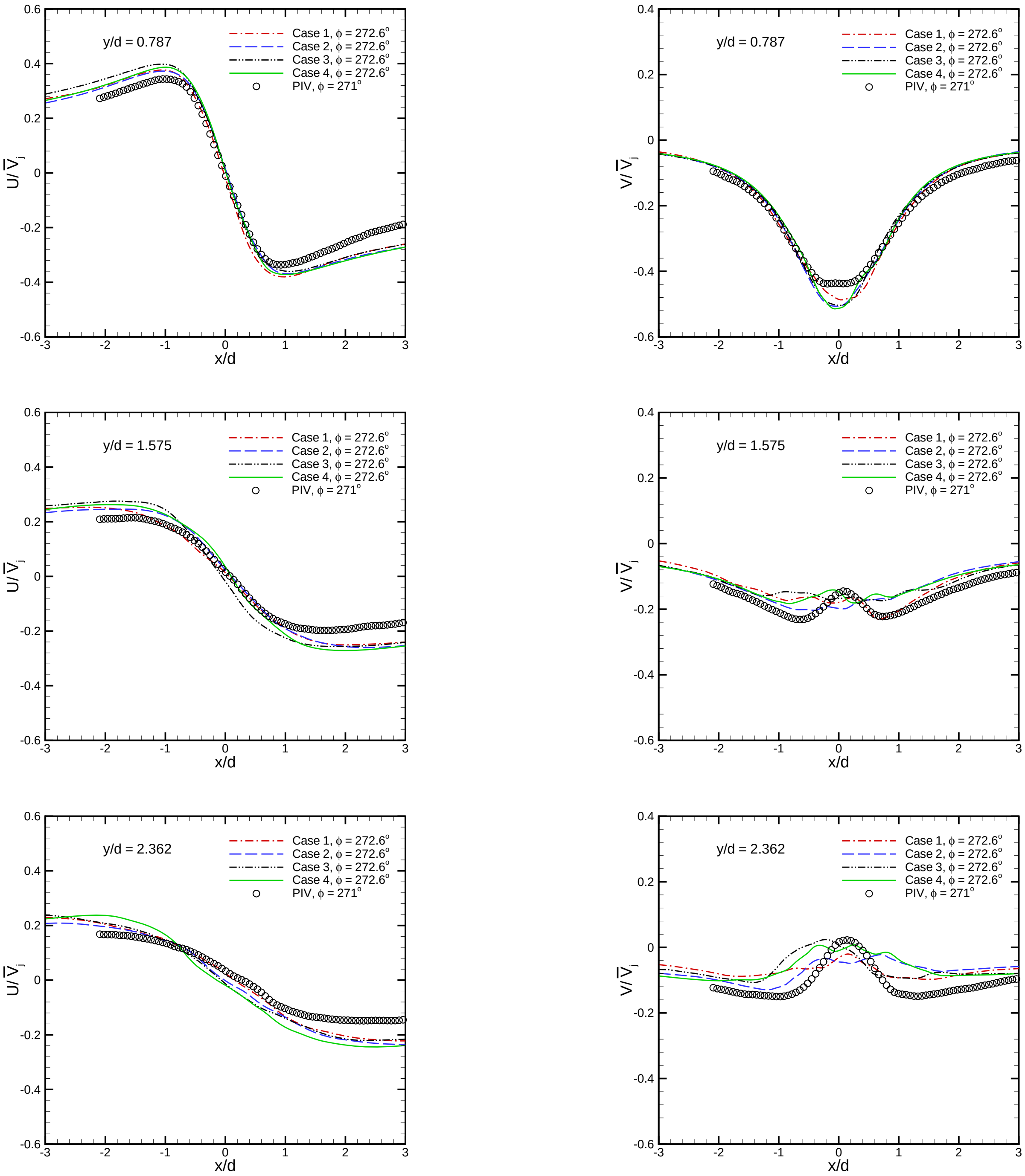

Figure 8. Plot of phase-averaged u- and v-velocity profiles along the horizontal lines $y/d = 0.787$, $y/d = 1.574$ and $y/d = 2.362$, above the jet exit plane at phase angle $\phi \approx 270^o$.

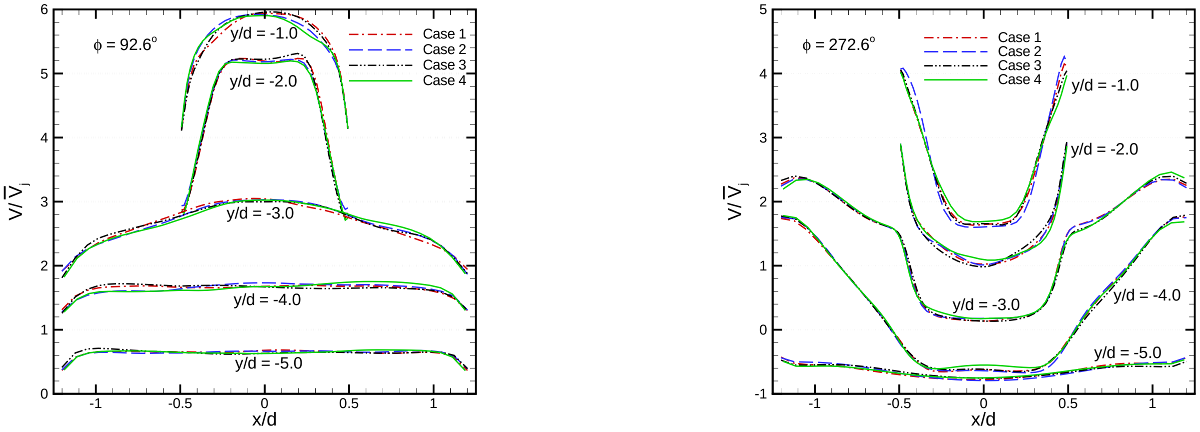

Figure 9. Plot of phase-averaged v-velocity profile along the horizontal lines in the slot ($y/d = -1.0$ and -2.0) and the cavity ($y/d = -3.0$, -4.0 and -5.0) at phase angles $\phi \approx 90^o$ and $\phi \approx 270^o$. Profiles at $y/d = -4.0$, -3.0, -2.0 and -1.0 are shifted up along the ordinate by 1, 2, 3 and 4 units, respectively, from that at $y/d = -5.0$.

the computed profiles as compared to the measurements. The cross stream distributions of the time-averaged u- and v-velocity profiles are shown in figure 11 on the next page at three stations ($y/d \approx 0.787$, 1.575 and 2.362) above the jet exit plane. While the computed $< u >$-velocity profiles consistently show higher values than the measurements outside the core region of the jet at all stations, the computed $< v >$-velocity profiles closely match the experiments except for the lower values along the jet centerline as compared to the measurements. Time-averaged v-velocity profiles at five stations in the slot and the cavity are shown in figure 12 on page 15. It is interesting to note that while the velocity in the shear layer at $y/d \approx -1$ is positive, the velocity is negative in the shear layer at $y/d \approx -2$ implying that somewhere in between these two stations, the mean cross stream distribution is zero across the slot since the net mass flux is zero. In the cavity, $< v >$-velocity is positive in the shear layer at all three stations, whereas it is negative in the core.

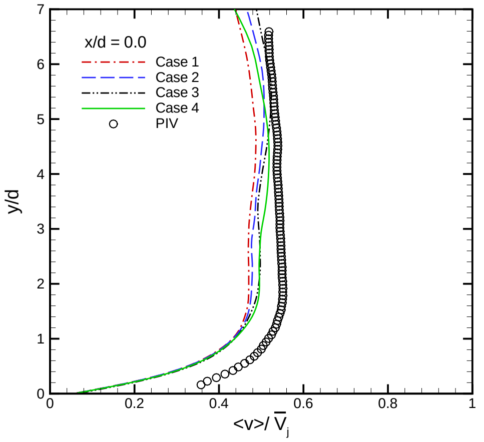

Figure 10. Plot of time-averaged v-velocity profile along the vertical centerline $x/d = 0.0$ above the jet exit plane.

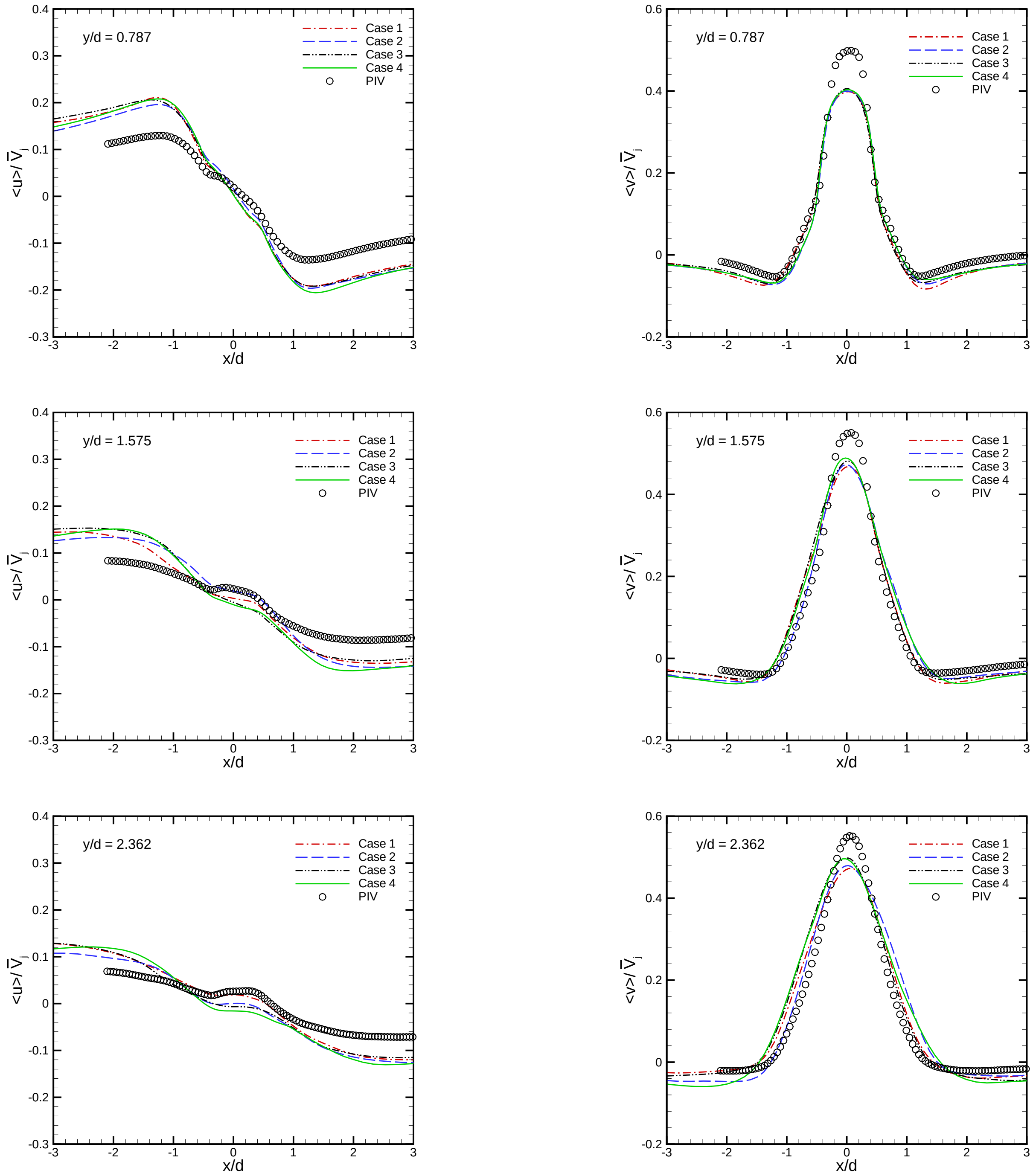

Figure 11. Plot of time-averaged u- and v-velocity profiles along the horizontal lines $y/d = 0.787$, $y/d = 1.574$ and $y/d = 2.362$, above the jet exit plane.

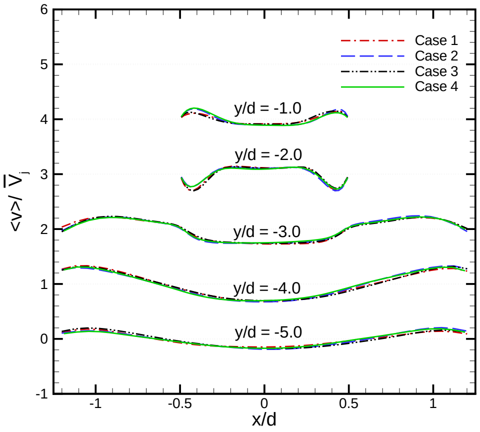

Figure 12. Plot of time-averaged v-velocity profile along the horizontal lines in the slot ($y/d = -1.0$ and -2.0) and the cavity ($y/d = -3.0$, -4.0 and -5.0). Profiles at $y/d = -4.0$, -3.0, -2.0 and -1.0 are shifted up along the ordinate by 1, 2, 3 and 4 units, respectively, from that at $y/d = -5.0$.

We now focus on the temporal variations and the frequency spectra of v-velocity at several stations along the jet centerline for Case 4. At any given (x, y) location, the frequency spectrum is obtained by computing the average of the spectra at several (but not all) grid points in the homogeneous spanwise direction. Figure 13 on the next page shows the temporal variations of the streamwise velocity (v), the phase averages of the streamwise velocity (V) and the corresponding velocity fluctuations (v'') at eight different streamwise locations along the jet centerline in the symmetry plane ($z = 0$). The instantaneous streamwise velocity is averaged in 24 phase bins, and the corresponding velocity fluctuations are obtained by subtracting the linearly-interpolated phase averages from the instantaneous velocity. The temporal variations in the near-field ($y/d \approx 0$ to 4) show more intense velocity fluctuations (v'') during the blowing phase of the cycle than during the suction phase indicating that suction of the ambient fluid into the narrow slot has a tendency to stabilize the flow in the near-field. Also, in the slot ($y/d \approx -1$ and -2), the velocity variation is mostly sinusoidal and the velocity fluctuations are spread almost uniformly over the entire cycle. Furthermore, the frequency spectra corresponding to the variations of v'' at these stations are shown in figures 14 and 15 on page 17. It should be noted that the temporal variations shown in figure 13 correspond to fixed spanwise stations whereas the frequency spectra are obtained by averaging the individual spectra at a particular (x, y) location across the span. The frequency ($\omega_\kappa = 2\pi f \kappa$, where κ is the wave number) in these plots is non-dimensionalized by $\bar{V}_j/d$ and the spectrum $E_{vv}(\omega_\kappa)$ is obtained by normalizing the spectral density by $2\pi f$. Also included in these plots are the lines corresponding to $\kappa^{-5/3}$ and κ^{-7} variations. Whereas the $\kappa^{-5/3}$ variation is associated with the inertial subrange,[29] the κ^{-7} variation on the other hand characterizes the dissipation range[30] where most of the turbulent kinetic energy is dissipated by the action of the viscosity. A noticeable inertial subrange and dissipation range in the spectra at $y/d \approx 1$, 2 and 3 in figure 14 indicates a well-developed turbulent flow at these stations. Since the Reynolds number is not very large, the dissipating eddies are only slightly smaller than the energy-containing eddies and so the inertial subrange is quite narrow at $y/d \approx 0$ and broadens as one moves away from the jet exit plane. In the cavity at $y/d \approx -4$, the spectrum shown in figure 15 depicts a relatively short inertial subrange and a distinct dissipation range associated with the turbulent flow at this station. However, as one moves up towards the slot, the inertial range narrows further and the dissipation range departs from the -7 slope. This is consistent with the earlier observation that flow laminarizes as it accelerates into the slot from the cavity.

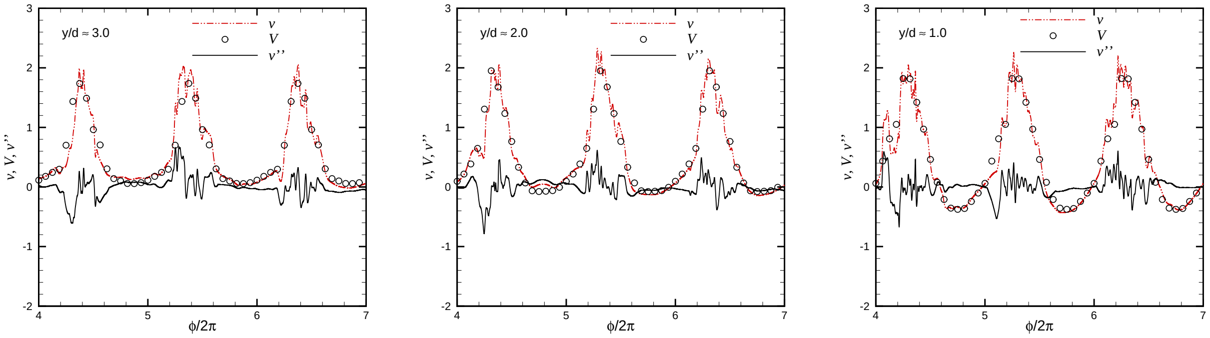

(a) $y/d \approx 3.0$

(b) $y/d \approx 2.0$

(c) $y/d \approx 1.0$

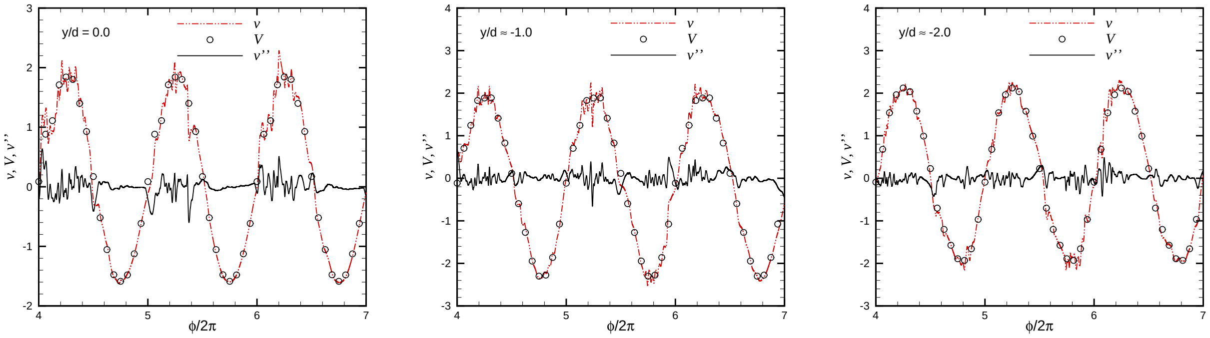

(d) $y/d \approx 0.0$

(e) $y/d \approx -1.0$

(f) $y/d \approx -2.0$

(g) $y/d \approx -3.0$

(h) $y/d \approx -4.0$

Figure 13. Temporal variation of instantaneous v-velocity, phase-averaged v-velocity and turbulent fluctuation v'' obtained for Case 4 at various locations along the centerline in the symmetry plane.

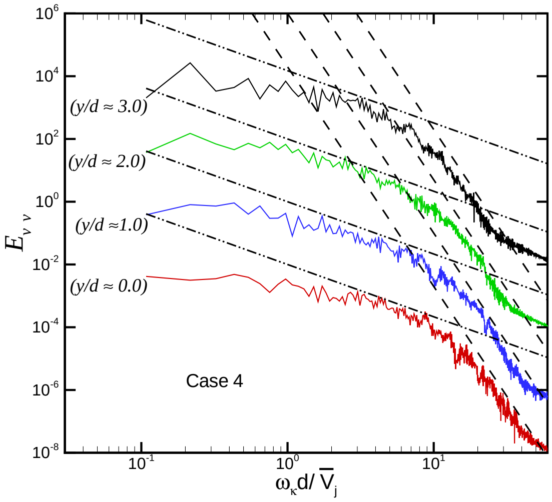

Figure 14. **Frequency spectra corresponding to turbulent fluctuations v'' along the centerline at $y/d \approx 0.0, 1.0, 2.0$ and 3.0 for Case 4. Note that the spectrum at $y/d \approx 1.0, 2.0$ and 3.0 is shifted up by two, four and six decades, respectively, from that at $y/d = 0.0$. Dash-dot-dot and dashed lines correspond to $\kappa^{-5/3}$ and κ^{-7} variations, respectively.**

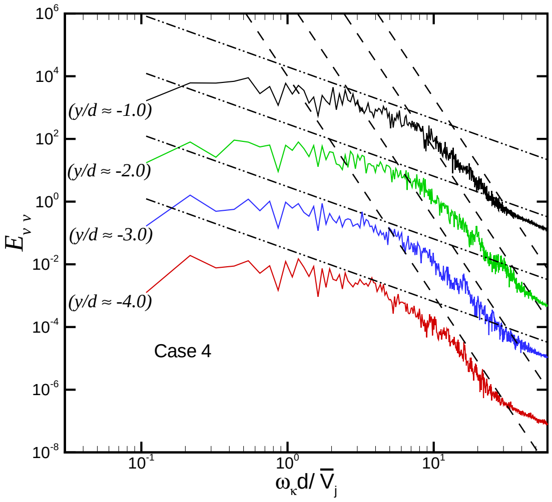

Figure 15. **Frequency spectra corresponding to turbulent fluctuations v'' along the centerline at $y/d \approx -1.0, -2.0, -3.0$ and -4.0 for Case 4. Note that the spectrum at $y/d \approx -3.0, -2.0$ and -1.0 is shifted up by two, four and six decades, respectively, from that at $y/d = -4.0$. Dash-dot-dot and dashed lines correspond to $\kappa^{-5/3}$ and κ^{-7} variations, respectively.**

IV. Conclusions

The evolution of three-dimensional transitional synthetic jets in initially quiescent air is studied using direct numerical simulations. Flow visualizations indicate that the near-field is dominated by counter-rotating vortex pairs that convect downstream by self-induction. The results also show the presence of rib-like secondary vortical structures in the streamwise direction surrounding the cores of the primary vortex pair. These secondary structures undergo rapid amplification due to three-dimensional vortex stretching and cause transition of the primary vortex pair into a well-developed turbulent jet within a short distance from the orifice. The cross stream distributions of phase-averaged and time-averaged velocity components from the calculations compare reasonably well with the experiments, eventhough the time-averaged streamwise velocity along the centerline is lower in the computations than in the experiments. Also, higher values of time-averaged cross stream velocities outside the core region of the jet in the computations suggest a stronger entrainment as compared to the measurements. The ambient fluid above the slot exit and the fluid in the cavity tend to laminarize as the flow accelerates into the narrow slot during the suction and blowing phases of the cycle. Frequency spectra in the cavity also corroborates this observation. Spectral analysis in the near-field indicates a discernible inertial subrange and distinct dissipation range associated with a fully-developed turbulent jet within a short distance from the exit plane.

Acknowledgments

This work is supported by National Aeronautics and Space Administration (Grant NAG-1-01024) and U.S. Air Force Office of Scientific Research (Grant F49620-03-1-0146).

References

[1] Smith, B. L. and Glezer, A., "Jet Vectoring Using Synthetic Jets," *J. Fluid Mech.*, Vol. 458, 2002, pp. 1–34.

[2] Rathnasingham, R. and Breuer, K. S., "System Identification and Control of a Turbulent Boundary Layer," *Phys. Fluids A*, Vol. 9, No. 7, 1997, pp. 1867–1869.

[3] Rathnasingham, R. and Breuer, K. S., "Active Control of Turbulent Boundary Layers," *J. Fluid Mech.*, Vol. 495, 2003, pp. 209–233.

[4] Lee, C. Y. and Goldstein, D. B., "DNS of Microjets for Turbulent Boundary Layer Control," AIAA Paper 2001–1013, June 2001.

[5] Wygnanski, I., "Boundary Layer and Flow Control by Periodic Addition of Momentum," AIAA Paper 97–2117, 1997.

[6] Smith, D., Amitay, M., Kibens, V., Parekh, D., and Glezer, A., "Modification of Lifting Body Aerodynamics Using Synthetic Jet Actuators," AIAA Paper 98–0209, 1998.

[7] Amitay, M., Kibens, V., Parekh, D., and Glezer, A., "The Dynamics of Flow Reattcahment Over a Thick Airfoil Controlled by Synthetic Jet Actuators," AIAA Paper 99–1001, June 1999.

[8] Crook, A., Sadri, A. M., and Wood, N. J., "The Development and Implementation of Synthetic Jets for the Control of Separated Flow," AIAA Paper 99–3176, June 1999.

[9] Smith, B. L. and Glezer, A., "Vectoring and Small-Scale Motions Effected in Free Shear Flows Using Synthetic Jet Actuators," AIAA Paper 97–0213, 1997.

[10] Amitay, M., Honohan, A., Trautman, M., and Glezer, A., "Modification of the Aerodynamic Characteristics of Bluff Bodies Using Fluidic Actuators," AIAA Paper 97–2004, June 1997.

[11] Meissner, A., "Uber Piezo-Elektrische Kristalle bei Hoch-Frequenz," *Zh. Tekh. Fiz*, Vol. 7, 1926, pp. 585.

[12] Ingard, U. and Labate, S., "Acoustic Circulation Effects and the Nonlinear Impedance of Orifices," *J. Acoust. Soc. Am.*, Vol. 22, No. 2, 1950, pp. 211–218.

[13] Andres, J. M. and Ingard, U., "Acoustic Streaming at High Reynolds Numbers," *J. Acoust. Soc. Am.*, Vol. 25, No. 5, 1953, pp. 928–932.

[14] Mednikov, E. P. and Novitskii, B. G., "Experimental Study of Intense Acoustic Streaming," *Soviet Phys. Acoust.*, Vol. 21, No. 2, 1975, pp. 152–154.

[15] Lebedeva, I. V., "Experimental Study of Acoustic Streaming in the Vicinity of Orifices," *Soviet Phys. Acoust.*, Vol. 26, No. 4, 1980, pp. 331–333.

[16] Sheen, S. H., Lawrence, W. P., and Raptis, A. C., "Cavitation-Controlled Ultrasonic Agitator," *Proc. IEEE Ultrasonics Symposium*, Vol. 1, 1989, pp. 653–656.

[17] Smith, B. L. and Glezer, A., "The Formation and Evolution of Synthetic Jets," *Phys. Fluids*, Vol. 10, No. 9, 1998, pp. 2281–2297.

[18] Yao, C. S., Chen, F. J., Neuhart, D., and Harris, J., "Synthetic Jets in Quiescent Air," *Proc. NASA LaRC Workshop on CFD Validation of Synthetic Jets and Turbulent Separation Control*, Williamsburg, Virginia, March 29-31, 2004.

[19] Kral, L. D., Donovan, J. F., Cain, A. B., and Cary, A. W., "Numerical Simulation of Synthetic Jet Actuators," AIAA Paper 97–1824, June 1997.

[20] Rizzetta, D. P., Visbal, M. R., and Stanek, M. J., "Numerical Investigation of Synthetic-Jet Flowfields," *AIAA J.*, Vol. 37, No. 8, 1999, pp. 919–927.

[21] Mallinson, S. G., Hong, G., and Reizes, A. J., "Some Characteristics of Synthetic Jets," AIAA Paper 99–3651, June 1999.

[22] Lee, C. Y. and Goldstein, D. B., "Two-Dimensional Synthetic Jet Simulation," *AIAA J.*, Vol. 40, No. 3, 2002, pp. 510–516.

[23] utturkar, Y., Holman, R., Mittal, R., Carroll, B., Sheplak, M., and Cattafesta, L., "A Jet Formation Criterion for Synthetic Jet Actuators," AIAA Paper 2003–0636, 2003.

[24] Zang, Y., Street, R. L., and Kossef, J. R., "A non-staggered Grid, Fractional Step Method for Time-Dependent Incompressible Navier-Stokes Equations in Curvilinear Coordinates," *J. Comp. Phys.*, Vol. 114, 1994, pp. 18–33.

[25] Ye, T., Mittal, R., Udaykumar, H. S., and Shyy, W., "An Accurate Cartesian Grid Method for Viscous Incompressible Flows with Complex Immersed Boundaries," *J. Comp. Phys.*, Vol. 156, 1999, pp. 209–240.

[26] Leonard, B. P., "A Stable and Accurate Convection Modeling Procedure Based on Quadratic Upstream Interpolation," *Comput. Methods Appl. Mech. Engrg.*, Vol. 19, 1979, pp. 59–98.

[27] Najjar, F. M. and Mittal, R., "Simulations of Complex Flows and Fluid-Structure Interaction Problems on Fixed Cartesian Grids," *FEDSM2003–45577, Proc. FEDSM'03, 4th ASME-JSME Joint Fluids Engineering Conference*, Honolulu, Hawaii, 2003, pp. 184–196.

[28] Reynolds, W. C. and Hussain, A. K. M. F., "The mechanics of an organized wave in turbulent shear flow. Part 3. Theoretical models and comparisons with experiments," *J. Fluid Mech.*, Vol. 54, 1972, pp. 263–288.

[29] Tennekes, H. and Lumley, J. L., *A First Course In Turbulence*, MIT Press, 1972.

[30] Hinze, J. O., *Turbulence*, McGraw-Hill, 1975.